Imaging Carrier Inhomogeneities in Ambipolar Tellurene Field Effect Transistors

Samuel Berweger,[*,†,‡] Gang Qiu,[¶,§] Yixiu Wang,[‖] Benjamin Pollard,[‡] Kristen L. Genter,[†,⊥] Robert Tyrell-Ead,[†] T. Mitch Wallis,[†] Wenzhuo Wu,[‖,§] Peide D. Ye,[¶,§] and Pavel Kabos[†]

†*Applied Physics Division, National Institute of Standards and Technology, Boulder, CO*

‡*Department of Physics, University of Colorado, Boulder, CO*

¶*School of Electrical and Computer Engineering, Purdue University, West Lafayette, IN*

§*Birck Nanotechnology Center, Purdue University, West Lafayette, IN*

‖*School of Industrial Engineering, Purdue University, West Lafayette, IN*

⊥*Department of Mechanical Engineering, University of Colorado, Boulder, CO*

E-mail: samuel.berweger@nist.gov

Abstract

Developing van der Waals (vdW) homojunction devices requires materials with narrow bandgaps and simultaneously high hole and electron mobilities for bipolar transport, as well as methods to image and study spatial variations in carrier type and associated conductivity with nanometer spatial resolution. Here we demonstrate the general capability of near-field scanning microwave microscopy (SMM) to image and study the local carrier type and associated conductivity *in operando* by studying ambiploar field effect transistors (FETs) of the 1D vdW material tellurium in 2D form. To quantitatively understand electronic variations across the device, we produce nanometer resolved maps of the local carrier equivalence backgate voltage. We show that the

global device conductivity minimum determined from transport measurements does not arise from uniform carrier neutrality, but rather from the continued coexistence of p-type regions at the device edge and n-type regions in the interior of our micron-scale devices. This work both underscores and addresses the need to image and understand spatial variations in the electronic properties of nanoscale devices.

Keywords

Atomic Force Microscope, Microwave, Near-Field Microscopy, Field-Effect Transistor, 2D Materials

Developing fundamental circuit building blocks such as diodes and transistors[1] based on low-dimensional van der Waals (vdW) materials requires producing and controlling adjoining regions of p-type and n-type transport.[2–7] While the broad library or vdW materials offers a range of novel functionalities such as memristors,[8] topologically protected states,[9–11] or those based on magnetic[12] and other spin-based phenomena,[13] MoS_2 and the associated family of transition metal dichalcogenides (TMDs) remain the primary candidates for semiconducting applications. In these materials bipolar transport for homojunction devices can be difficult to achieve,[2,14] and difficult-to-fabricate heterostructures remain the primary practical path for pn junctions and other basic semiconducting circuit elements.[7] A key challenge therefore remains the development and discovery of new materials for homojunction devices with the narrow bandgaps and simultaneously high hole and electron mobilities[15–17] desired for bipolar transport.

Nanometer thin films of elemental tellurium have recently been demonstrated for device applications.[17] Tellurium is a vdW material whose helical 1D atomic chains can be assembled into 1D filaments[18] or 2D films (tellurene)[17,19] and deposited using solution-based processes. Tellurene in particular exhibits both n- and p-type mobilities as high as 700 $cm^2/V{\cdot}s$, and the thickness-dependent bandgap as small as 0.4 eV[17] readily enables bipolar transport.[20]

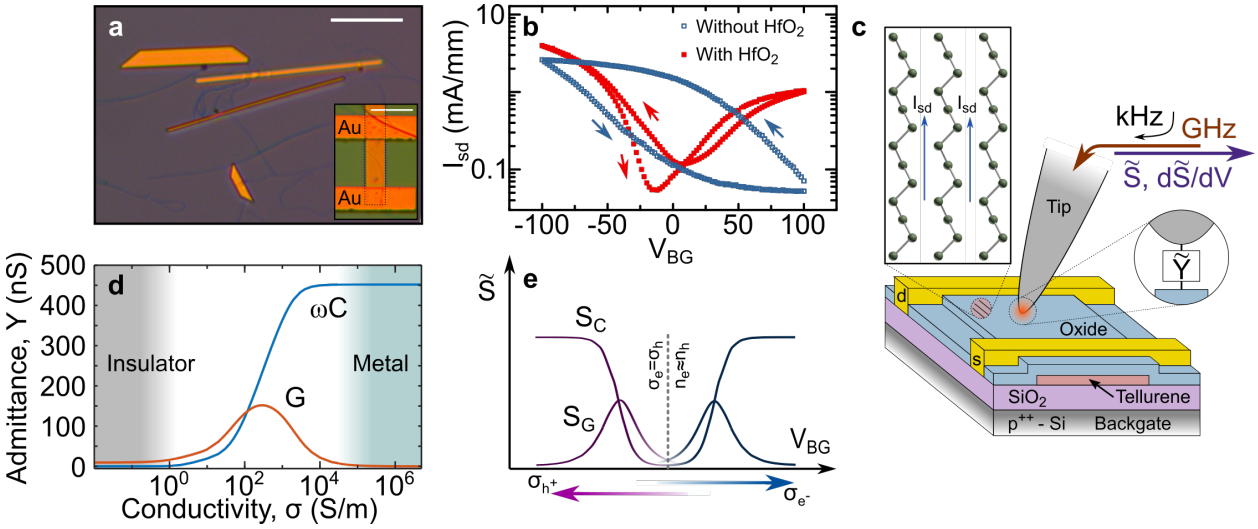

Figure 1: (a) Optical micrograph of solution-grown tellurene crystals showing characteristic trapezoidal shape as well as string-like Te filaments formed during process (scale bar: 20 μm). Inset: Optical micrograph of a tellurene device (scale bar: 8 μm). (b) Transport characteristics of a tellurene FET before and after deposition of a 10 nm conformal HfO_2 overcoat. (c) Schematic of the experimental setup illustrating the transport along the direction of the atomic Te chains. (d) Finite element modeling of the complex-valued tip-sample admittance $\tilde{Y} = G + i\omega C$ at 17.3 GHz as a function of tellurene conductivity. (e) Illustration of the expected measured microwave signal $\tilde{S} \propto \tilde{Y}$ as a function of V_{BG} for an ambipolar FET showing clear regimes of contrast corresponding to hole- and electron-conductivity.

Unlike black phosphorous, another promising material exhibiting bipolar transport,[15,16] tellurene is stable under ambient conditions and resistant to long-term deterioration. Dopant incorporation is often difficult in 2D vdW materials, and the solution-based synthesis of tellurene further offers an attractive avenue for doping, but successful exploitation of this feature requires a detailed understanding of the resulting local transport properties and their relation to growth conditions. It is thus of critical importance to be able to address and study not only the local carrier density and associated conductivity in functional devices with nanometer spatial resolution, but to be able to do so in a manner that is also sensitive to the carrier type.

An optical micrograph of representative trapezoidal tellurene flakes deposited on SiO_2 is shown in Fig. 1a). Also seen in the optical micrograph are the curved string-like 1D Te filaments that result as a by-product from solution growth.[18] After contact electrodes are

fabricated via electron beam lithography, devices are encapsulated in 10 nm of conformal oxide using atomic layer deposition (ALD) of either HfO_2 or Al_2O_3. Shown in Fig. 1b) is the backgate voltage (V_{BG})-dependent transport characteristic of a tellurene FET before and after ALD deposition, acquired with a source-drain bias of $V_{sd} = 0.05$ V. In addition to preventing device failure due to tip-sample conduction, the ALD encapsulation also reduces device hysteresis and enables bipolar transport,[20] likely due to oxygen vacancy-induced n-doping.[21]

An illustration of the experimental setup is shown in Fig. 1c) with the scanning microwave microscope (SMM, also called scanning microwave impedance microscopy, sMIM) based on an atomic force microscope (AFM) operating in contact mode that detects the phase-resolved real and imaginary components of the microwave signal $\tilde{S} = S_G + iS_C$. The simulated (COMSOL 4.2*) tip-sample admittance $\tilde{Y} = G + i\omega C$ for a unipolar tellurene device is shown in Fig. 1d) with the conductance G and capacitance C as a function of the tellurene conductivity $\sigma_i = n_i e \mu_i$ with the elementary charge e, carrier density n_i, and corresponding carrier mobility μ_i ($i = h, e$). Assuming $\tilde{S} \propto \tilde{Y}$ (i.e., $S_G \propto G$ and $S_C \propto C$),[22–24] the SMM sensitivity peaks at $\sigma = 300$ S/m yet remains sensitive over the range $\sigma \approx 10^0$ – 10^4 S/m. Controlling the carrier type and concentration using the global backgate V_{BG}, we expect the measured signal $\tilde{S}$ to evolve as schematically illustrated in Fig. 1e) with two distinct regions of sensitivity as the device transitions between the hole and electron transport regimes.

Shown in Fig. 2a) is an optical micrograph of a tellurene FET fabricated on 90 nm SiO_2, with source and drain electrodes as indicated and a channel length of 8 μm. Shown in Fig. 2b) is the source-drain current I_{sd} measured at $V_{sd} = \pm 0.05$ V, showing a clear global conductivity minimum (carrier equivalence) point at $V_{BG} = 20$ V separating the hole and electron transport regimes as indicated.

The contact-mode AFM topography in Fig. 2c) shows a uniform device with a thickness of ∼9 nm and only small topographic variations. Also visible are co-deposited Te filaments, including one over the device. A sequence of S_G and S_C images at select voltages are shown

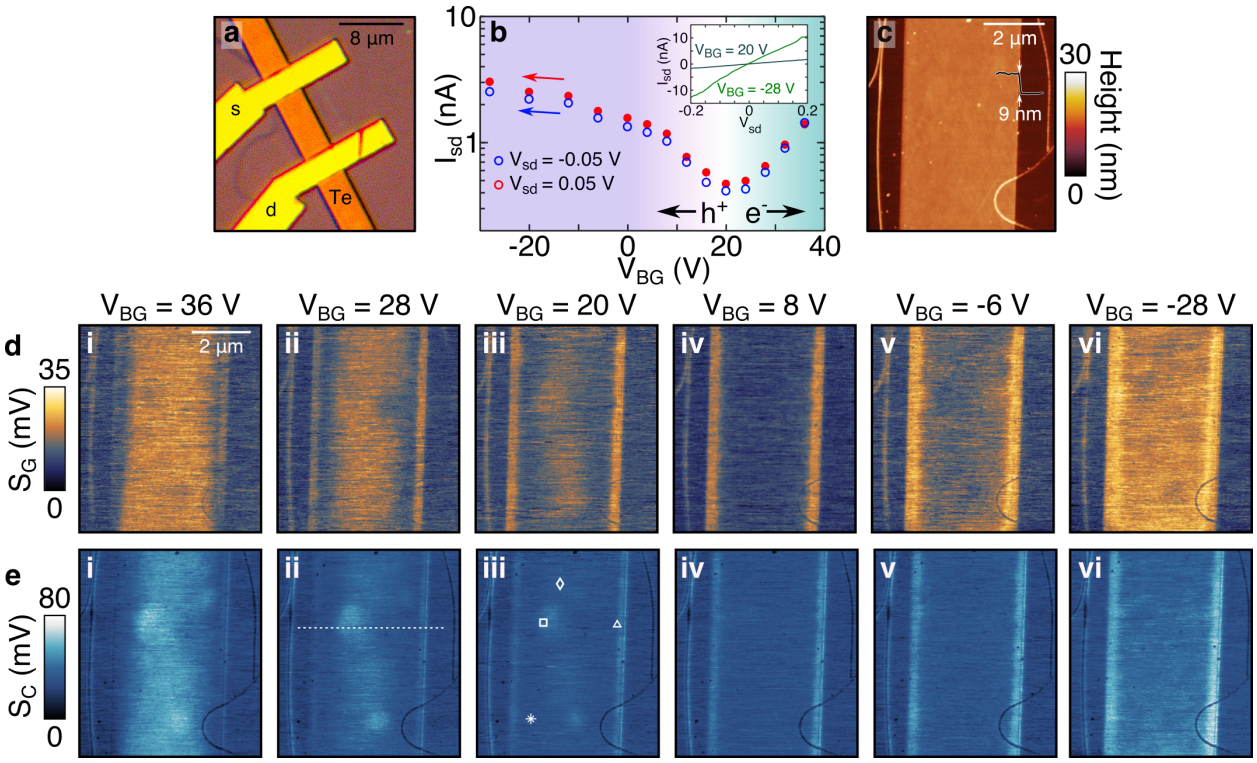

Figure 2: (a) Optical micrograph of an Al_2O_3-encapsulated tellurene device with source and drain electrodes as indicated. (b) Transport characteristics of the device, with the global device carrier equivalence point at V_{BG} = 20 V and electron and hole transport regimes as indicated. Inset: The IV characteristics of the device at V_{BG} as indicated with near-ohmic behavior, though some nonlinearity and increased noise are seen at positive V_{sd}. (c) Contact mode AFM topography of the device active area (source and drain electrodes are just out of view at image top and bottom). (d) and (e) show SMM images acquired at sequentially decreasing values of V_{BG} as indicated, with the conductance S_G and capacitive S_C channels, respectively.

in Fig. 2d) and e), respectively (see supporting information for full data set). For large and positive V_{BG} the device is in the electron-transport regime, and the higher signals in both channels indicate that the device interior is more conductive than the device edges. As V_{BG} decreases and approaches the global device carrier equivalence point at V_{BG} = 20 V, the interior of the device becomes less conductive while the edge conductivity increases. When V_{BG} is further decreased and the device transitions into the hole-conduction regime, we see the conductivity in the device interior reach a minimum at V_{BG} = 8 V while the edge conductivity continues to increase monotonically. As V_{BG} is decreased beyond the conductivity minimum of the device interior, the conductivity in this region is seen to increase

again, though over the voltage range accessible with this device it does not reach parity with the edges again. Observed differences between S_G and S_C in high-conductivity regions are expected, as the former does not increase monotonically with conductivity.

Several notable features stand out from the sequence of microwave near-field images. In particular, the device interior does show spatial conductivity variations. The filament also affects the measured signal, although this appears to be limited to reducing the overall signal due to the increased tip-sample spacing, and no electronic effects arise in its vicinity. Most importantly, the discrepancy in V_{BG}-dependent behavior between the device interior and exterior suggests inhomogeneities in the carrier type and we perform additional measurements to better understand this behavior.

Differential measurements are sensitive to the slope of the conductivity-dependent $\tilde{S}$ signal. Shown in Fig. 3a) are the $S'_C \equiv dC/dV_{tip}$ [22,25] images corresponding to the S_C images shown in Fig. 2d) and e) (see supporting information for full data set, including S'_G). The sign of S'_C directly reflects the carrier type locally present beneath the tip, and gives a direct measure of the local *p*- or *n*-type character of the tellurene device. For instance, over a *p*-type region the positive part of the V_{tip} modulation cycle locally depletes (repels) *p*-type carriers and thus reduces the conductivity, giving an out-of-phase response ($S'_C < 0$, blue regions). For the *n*-type regions the opposite will occur, where the positive portion of the cycle accumulates (attracts) *n*-type carriers and thus increases conductivity, yielding an in-phase response ($S'_C > 0$, red regions).

Together with S_C, S'_C provides a more comprehensive understanding of these devices. Shown in Fig. 3b) are the V_{BG}-dependent S_C and S'_C signals at the position of the corresponding symbols in Fig. 2e)iii) and Fig. 3a)iii). For the three positions within the device interior, S_C decreases with decreasing V_{BG}, reaches a minimum value at the local carrier equivalence point, and then increases again, while S'_C crosses zero (dashed lines) at the same V_{BG} values as the minima of S_C, confirming their differential relationship. At the device edge, S_C increases monotonically with decreasing V_{BG} while S'_C remains negative over the

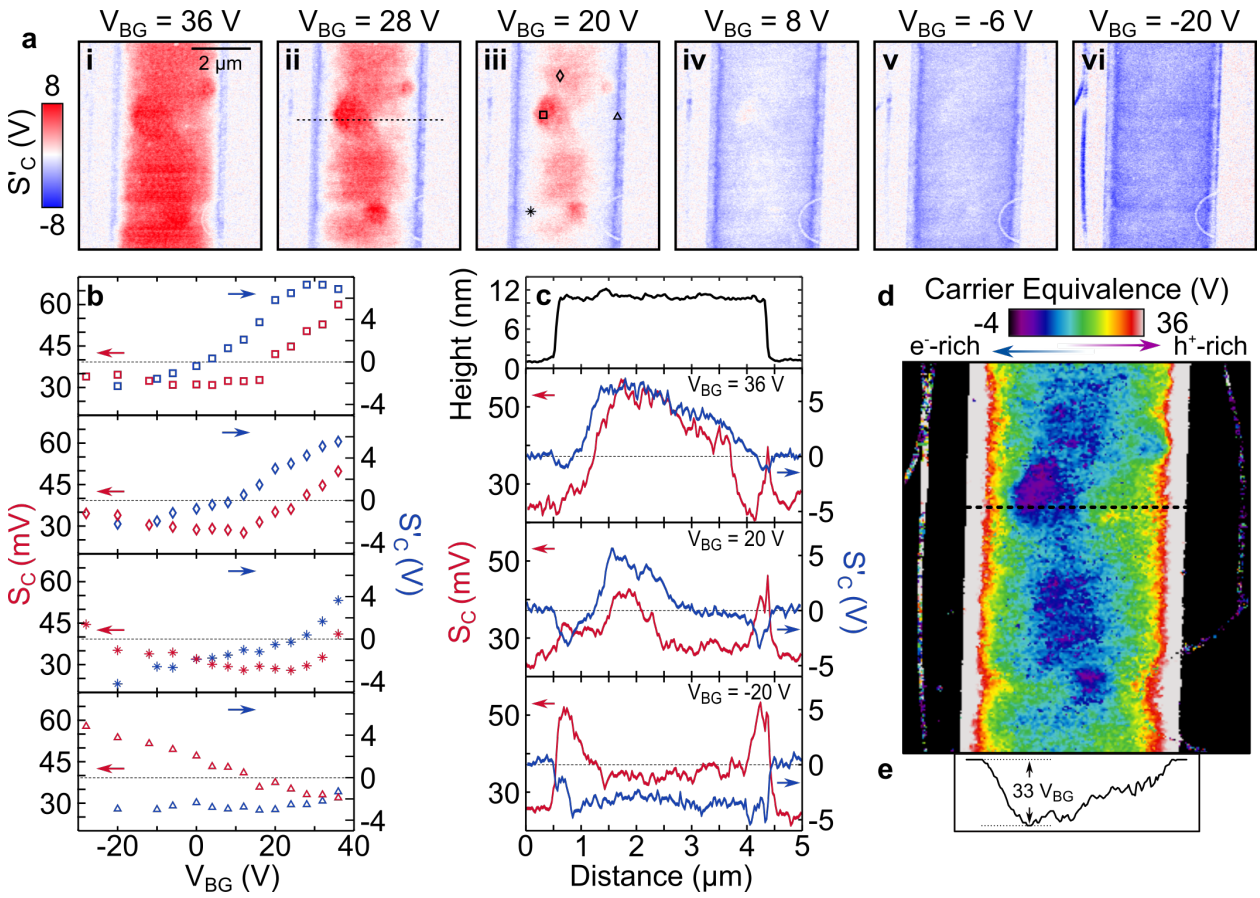

Figure 3: (a) S'_C images acquired at V_{BG} as indicated. (b) S'_C and S_C as a function of V_{BG} acquired at the locations of the corresponding symbols in a)iii) and Fig. 2e)iii). (c) Line cuts across the tellurene device showing the topography (top) and S'_C and S_C at values of V_{BG} as indicated, taken from the location of the dashed line in a)ii) and Fig. 2e)ii). Dashed lines in b) and c) are a guide to the eye at $S'_C = 0$ V. (d) Spatially resolved map of the local carrier equivalence voltage. (e) Line cut taken along the dashed line in d) showing a variation of $V_{BG} > 33$ V across the device.

full voltage range as expected.

We next take a closer look at the spatial variations in S'_C and S_C across the tellurene device. Shown in Fig. 3c) are line cuts taken at the position of the dashed line in Fig. 2e)ii) and Fig. 3c)ii) with the topography (top panel) and corresponding S'_C and S_C cuts at values of V_{BG} as indicated. At large positive bias the conductivity is highest in the interior of the crystal where the positive S'_C reflects the n-type behavior measured by transport while the edges appear weakly conductive with the negative S'_C signal, revealing p-type conductivity well above the global carrier equivalence point. At the global device carrier equivalence point

we see a clear coexistence between p-type behavior at the edges and spatially inhomogeneous n-type behavior within the device interior. Comparison with S_C reveals that the p-type edges are significantly more conductive than most of the device interior at this point, though over a significantly smaller area. Once the device has transitioned to uniform p-type behavior at V_{BG} = -20 V, the conductivity profile is inverted with higher conductivity near the edges, though clear inhomogeneities remain.

The device edge can experience enhanced local electric fields due to fringing and resulting concentration of the fields from the backgate. However, the strong p-type character at the edges cannot be explained by field fringing, where the enhancement of the electric field from the global backgate at the crystal edges would reduce the hole density at positive backgate biases relative to the device interior, contrary to observations. Similarly, modification and enhancement of the tip-sample fields are possible with the tip positioned at the edge of the crystal. Our estimated spatial resolution of <60 nm (see supporting information) provides the lateral distance over which the tip-edge interaction is expected to decay as the tip moves toward the device interior. The edge conductivity variations persist for several 100 nm from the edge and thus originate from material properties rather than effects of local field concentration at the device edges.

In order to fully understand the variations in carrier type we construct a nanometer-resolved carrier equivalence voltage map. To take advantage of the improved contrast of lock-in detection and to avoid uncertainty in the location of the S_C minima, we interpolate the V_{BG}-dependent zero crossing of S'_C to determine the local carrier equivalence point. Shown in Fig. 3d) is a spatially resolved map of the local carrier equivalence voltage at each spatial pixel in S'_C as determined from the full sequence of images (see supporting information).[26] This carrier equivalence map reveals the complex variations in carrier type and density across the device. Note that white regions at the device edges have a carrier equivalence point greater than 36 V_{BG}. The line cut along the dashed line in Fig. 3d), shown in Fig. 3e), underscores the degree of spatial inhomogeneity across the device with lateral

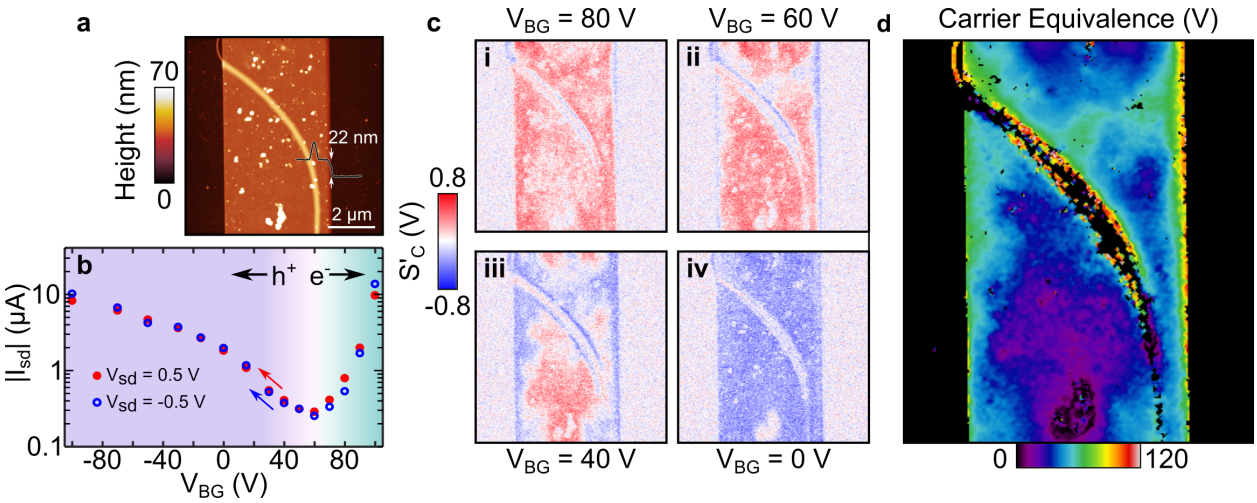

Figure 4: (a) AFM topography of a tellurene device with embedded Te filament. (b) Transport characteristics of the device with a global carrier equivalence point of $V_{BG} = 60$ V. (c) Sequence of S'_C images that illustrates the high degree of spatial inhomogeneity in carrier type and density present in this device as further seen in (d), the extracted carrier equivalence map.

variation in the local equivalence point of $V_{BG} > 33$ V.

While thin devices are largely uniform along the transport axis (see supporting information for an additional device), large variations in behavior are seen for other devices. Shown in Fig. 4a) is the AFM topography of a device where a tellurene filament is embedded beneath the crystal. This device, encapsulated with HfO_2, is deposited on 300 nm of SiO_2, which results in a lower backgate efficiency that requires larger voltages up to $V_{BG} = \pm 100$ V, and has a global carrier equivalence point of $V_{BG} = 60$ V as shown in Fig. 4b). The S'_C sequence in Fig. 4c) shows the evolution of the conductivity from *n*-type to *p*-type, with higher hole density at the device edges and an overall electron-rich interior. However, the embedded filament induces a large degree of spatial inhomogeneity within the crystal, as underscored by the carrier equivalence map shown in Fig. 4d).

The origin of the spatial variations in conductivity seen across these devices, most notably the significant differences between the edges and interior, is likely associated with several factors. One of the defining features of vdW materials is the capability of the weak interlayer interactions to accommodate the intercalation of dopants,[27,28] and growth kinetics may favor

incorporation of different types or concentrations of p-dopants later in the growth process when the edge termination is formed. We also observe that all images, including the carrier equivalence maps, show local spatial variations in electronic behavior on 10s of nanometer length scales. While these weakly correlate with structure in the topography (see supporting information), the possible influence of vdW assembly, including molecular alignment and possibly interfacial effects, is hard to discern due to the indistinguishability of underlying crystal features from thickness variations in the ALD overcoat. We note the prevalent strong p-type character and associated high local carrier equivalence voltage within the device interior near the embedded Te filament. This region immediately adjacent to the filament likely experiences significant tensile strain that appears to produce similar electrical characteristics to the edges. This suggests that strain strongly influences the carrier density and type. As the filaments appear to have p-type character, it is also possible that the filament induces local p-doping, although the region immediately on top of the embedded filament as well as the vicinity of filaments on top of devices do not appear p-type. Lastly, although n-type doping due to the ALD overcoat[20,21] would be expected to be stronger at the edges where the surface-to-volume ratio is higher, we cannot rule out interfacial impurities and associated fermi-level pinning as contributing factors.

The capability to study and image local variations in conductivity with nanometer spatial resolution has been a long-standing challenge for scanning probe methods. Optical near-field methods can be used to study conductivity variations in highly doped materials,[29] and while related near-field photocurrent microscopy has shown potential for graphene[30] its general application has not been explored. In particular, the differential implementations of SMM and closely related scanning capacitance microscopy (SCM) have previously been used to study the local carrier type in model systems.[22,25,31] On the other hand, conventional SMM can be used to study nanoscale devices[24,32] but has not yet been applied to ambipolar devices.

Studying devices *in operando* requires non-destructive probing in a compatible geometry, and AFM-based methods such as kelvin probe force microscopy[33,34] or conductive-AFM[35]

are well suited for such measurements. However, device encapsulation to prevent destructive electrical discharge from the tip precludes the use of these methods. This work is thus enabled by leveraging the subsurface imaging capability of SMM[24,36] and combining for the first time the conductivity sensing capability of the $\tilde{S}$ signal and the carrier-specific imaging of $\tilde{S}'$ to study bipolar transport in active devices.

Here we have shown how the unique capabilities of microwave near-field microscopy can be used to study the spatial variations in electronic properties of ambiploar field effect transistors. In addition to the established capability to image and study spatial variations in sample conductivity, we use differential imaging to determine the local carrier type throughout the backgate voltage-controlled evolution of the device transport properties. We find large variations in our tellurene devices, with strong p-type conductivity observed at the edge of all devices and lower p-type conductivity in the device interior that can readily be switched to n-type behavior at positive backgate biases. Our measurements reveal that global transport measurements belie the nanoscale complexity of the device, where we show that the device-average carrier equivalence point is actually the result of the simultaneous coexistence of p-type and n-type regions that give rise to an overall minimum conductivity rather than true carrier neutrality. We identify significant variations in the local carrier equivalence point across active devices due to structural variations, interfacial effects, as well as the influence of local strain. These results underscore the importance of understanding local variations in carrier density and type, and provide a direct means to evaluate the intercalation of dopants into vdW materials. Our approach can be broadly used to understand and guide the development of low-dimensional semiconducting device architectures and functionalities based on bipolar transport that can be controlled or switched by applied strain or other stressors.

Methods. Tellurene devices studied here are fabricated as described previously.[17] Tellurene films are grown by a solution-based process and deposited using a Langmuir-Blodgett process onto p^{++}-Si substrates covered by thermally deposited silicon dioxide, and contact

electrodes are fabricated via electron beam lithography. Devices are subsequently encapsulated in 10 nm of conformal oxide (HfO_2 or Al_2O_3) using atomic layer deposition. The devices are then mounted to the AFM scanner and the leads wirebonded to enable electrical measurements and backgate voltage control *in situ*.

The SMM is based on a modified commercial AFM/SMM system (Keysight*) operating in contact mode.[22] The microwave signal at ∼17.3 GHz is sourced from a vector network analyzer and delivered via the tip to the sample using a coaxial resonator, and the reflected $\tilde{S}$ signal is detected using an IQ mixer (Analog Devices*). A phase controlled reference signal is used to separate the real and imaginary components $\tilde{S} = S_G + iS_C$. Differential measurements are performed by applying an AC tip bias V_{tip} at a frequency of 50 kHz and an amplitude of $V_{p-p} = 1$ V. Lock in detection of the analog output of the IQ mixer yields the differential signals $S'_G \equiv dG/dV_{tip}$ and $S'_C \equiv dC/dV_{tip}$.[22,25]

We note that the differential relationship between $\tilde{S}'$ and $\tilde{S}$ suggests that a single measurement would be sufficient and the other data channel can be determined via numerical integration or differentiation at each spatial pixel. However, differential operations performed on a sequence of scans significantly increase the noise and are highly susceptible to sample drift. In principle, if sufficient stability is achieved the higher contrast in $\tilde{S}'$ could enable integration, though large backgate voltages beyond device breakdown would nevertheless be required to establish the constant of integration.

While these devices are hysteretic, we find that systematic V_{BG}-dependent measurement sequences can yield a high degree of reproducibility. In particular, we achieve this by sequentially acquiring single SMM images at each decreasing value of V_{BG} followed by a current-voltage (IV) sweep. We note that the device global conductivity minimum extracted from the sequence of IV curves corresponds to the condition where $\sigma_e = \sigma_h$. However, measurements of both field effect[20] and low-temperature Hall mobilities[19] suggest that $\mu_e \approx \mu_h$ along the atomic chains, and theoretical work[37] suggests comparable effective masses and thus mobilities for electrons and holes across the atomic chains as well. While the microwave

near-field probes transport both across and along the atomic chains, the conductivity minimum thus also corresponds approximately to the carrier equivalence (charge neutrality) point.

The conductivity-dependent microwave signal was simulated using COMSOL 4.2 in an approach previously validated for nanoscale systems in general[23] and 2D materials in particular.[22,24,36] The AC/DC package was used at a frequency of 17.3 GHz with an axisymmetric geometry with a semi-infinite sample to minimize computation times. The geometry consisted of a metallic parabolic tip with a radius of 20 nm in contact with a 10 nm film of Al_2O_3 ($\epsilon = 10$) covering a 9 nm thick sample of varying conductivity (Te crystal) that is separated from the conductive Si backgate ($\sigma = 10^4$ S/m) by 90 nm SiO_2 ($\epsilon = 3.9$).

Acknowledgments

We would like to thank Kevin J. Coakley for valuable discussions. The work at Purdue University is partly supported by NSF grant no. CMMI-1663214 and the Army Research Office under grant nos. W911NF-15-1-0574 and W911NF-17-1-0573

*Mention of commercial products is for informational purposes only, it does not imply NIST's recommendation or endorsement. Contributions of the National Institute of Standards and Technology, not subject to copyright in the United States.

Supporting Information

We provide the full data sets for all scans, data for an additional homogeneous device, and a high-resolution scan of a device. This material is available free of charge via the Internet at http://pubs.acs.org.

References

(1) Sze, S.; Ng, K. *Semiconductor Devices*; John Wiley & Sons, 2007.

(2) Ross, D. S.; Klement, P.; Jones, A. M.; Ghimire, N. J.; Yan, J.; Mandrus, D. G.; Taniguchi, T.; Watanabe, K.; Yao, W.; Cobden, D. H.; Xu, X. *Nat. Nanotech.* **2014**, *9*, 268.

(3) Pospischil, A.; Furchi, M. M.; Mueller, T. *Nat. Nanotechnol.* **2014**, *9*, 257.

(4) Baugher, B. W. H.; Churchill, H. O. H.; Yang, Y.; Jarillo-Herrero, P. *Nat. Nanotechnol.* **2014**, *9*, 262.

(5) Buscema, M.; Groenendijk, D. J.; Steele, G. A.; van der Zant, H. S. J.; Castellanos-Gomez, A. *Nat. Comms.* **2014**, *5*, 4651.

(6) Duan, X.; Wang, C.; Shaw, J. C.; Cheng, R.; Chen, Y.; Li, H.; Wu, X.; Tang, Y.; Zhanbg, Q.; Pan, A.; Jiang, J.; Yu, R.; Huang, Y.; Duan, X. *Nat. Mater.* **2014**, *9*, 1024.

(7) Liu, Y.; Weiss, N. O.; Duan, X.; Cheng, H. C.; Huang, Y.; Duan, X. *Nat. Rev. Mater.* **2016**, *1*, 16042.

(8) Sangwan, V. K.; Lee, H. S.; Bergeron, H.; Balla, I.; Beck, M. E.; Chen, K. S.; Hersam, M. C. *Nature* **2018**, *554*, 500.

(9) Kou, L.; a S. C. Wu,; Felser, C.; Frauenheim, T.; Chen, C.; Yan, B. *ACS Nano* **2014**, *8*, 10448.

(10) Ju, L.; Shi, Z.; Nair, N.; Lv, Y.; Jin, C.; Velasco Jr., J.; Ojeda-Aristizabal, C.; Bechtel, H. A.; Martin, M. C.; Zettl, A.; Analytis, K.; Wang, F. *Nature* **2015**, *520*, 650.

(11) Zhang, H.; Liu, C. X.; Qi, X. L.; Dai, X.; Fang, Z.; Zhang, S. C. *Nat. Phys.* **2009**, *5*, 438.

(12) Huang, B.; Clark, G.; Klein, D. R.; MacNeill, D.; Navarro-Moratalla, E.; Seyler, K. L.; Wilson, N.; McGuire, M. A.; Cobden, D. H.; Xiao, D.; Yao, W.; Jarillo-Herrero, P.; Xu, X. *Nat. Nanotechnol.* **2018**, *13*, 544.

(13) Mak, K. F.; McGill, K. L.; Park, J.; McEuen, P. L. *Science* **2014**, *344*, 1489.

(14) Chen, J. W.; Lo, S. T.; Ho, S. C.; Wong, S. S.; Vu, T. H. Y.; Zhang, X. Q.; Liu, Y. D.; Chiou, Y. Y.; Chen, Y. X.; Yang, Y. C.; et al. *Nature Comms.* **2018**, *9*, 3143.

(15) Das, S.; Demarteau, M.; Roelofs, A. *ACS Nano* **2014**, *8*, 11730.

(16) Liu, H.; Neal, A. T.; Zhu, Z.; Luo, Z.; Xu, X.; Tománek, T.; Ye, P. D. *ACS Nano* **2014**, *8*, 4033.

(17) Wang, Y.; Qiu, G.; Wang, R.; Huang, S.; Wang, Q.; Liu, Y.; Du, Y.; Goddard III, W. A.; Kim, M. J.; Xu, X.; Ye, P. D.; Wu, W. *Nat. Electron.* **2018**, *1*, 228.

(18) Mayers, B.; Xia, Y. *J. Mater. Chem.* **2002**, *12*, 1875.

(19) Du, Y.; Qiu, G.; Wang, Y.; Si, M.; Xu, X.; Wu, W.; Ye, P. D. *Nano Lett.* **2017**, *17*, 3965.

(20) Qiu, G.; Si, M.; Wang, Y.; Lyu, X.; Wu, W.; Ye, P. D. High-performance few-layer tellurium CMOS devices enabled by atomic layer deposited dielectric doping technique. 2018 76th Device Research Conference (DRC). 2018; pp 1–2.

(21) Valsaraj, A.; Chang, J.; Rai, A.; Register, L. F.; Banerjee, S. K. *2D Mater.* **2015**, *2*, 045009.

(22) Berweger, S.; Weber, J. C.; John, J.; Velazquez, J. M.; Pieterick, A.; Sanford, N. A.; Davydov, A. V.; Brunschwig, B.; Lewis, N. S.; Wallis, T. M.; Kabos, P. *Nano Lett.* **2015**, *15*, 1122.

(23) Lai, K.; Peng, H.; Kundhikanjana, W.; Schoen, D. T.; Xie, C.; Meister, S.; Ciu, Y.; Kelly, M. A.; Shen, Z. X. *Nano Lett.* **2009**, *9*, 1265.

(24) Wu, D.; Li, X.; Wu, X.; Li, W.; Yogeesh, M. N.; Ghosh, R.; Chu, Z.; Akinwande, D.; Niu, Q.; Lai, K. *Proc. Natl. Acad. Sci.* **2016**, *113*, 8583.

(25) Huber, H. P.; Humer, I.; Hochleitner, M.; Fenner, M.; Moertelmaier, M.; Rankl, C.; Imtiaz, A.; Wallis, T. M.; Tanbakuchi, H.; Hinterdorfer, P.; Kabos, P.; Smoliner, J.; Kopanski, J. J.; Kienberger, F. *J. Appl. Phys.* **2012**, *111*, 014301.

(26) Pollard, B.; Muller, E. A.; Hinrichs, K.; Raschke, M. B. *Nat. Comms.* **2014**, *5*, 3587.

(27) Bediako, D. K.; Rezaee, M.; Yoo, H.; Larson, D. T.; Zhao, S. Y. F.; Taniguchi, T.; Watanabe, K.; Brower-Thomas, T. L.; Kaxiras, E.; Kim, P. *Nature* **2018**, *558*, 425.

(28) Xiong, F.; Wang, H.; Liu, X.; Sun, J.; Brongersma, M.; Pop, E.; Cui, Y. *Nano Lett.* **2015**, *15*, 6777.

(29) Ritchie, E.; Hill, D. J.; Mastin, T. M.; Deguzman, P. D.; Cahoon, J. F.; Atkin, J. M. *Nano Lett.* **2017**, *17*, 6591.

(30) Woessner, A.; Alonso-González, P.; Lundeberg, M. B.; Gao, Y.; Barrios-Vargas, J. E.; Navickaite, G.; Ma, Q.; Janner, D.; Watanabe, K.; Cummings, A. W.; et al. *Nat. Comms.* **2016**, *7*, 10783.

(31) Edwards, H.; Ukraintsev, V. A.; San Martin, R.; Johnson, F. S.; Menz, P.; Walsh, S.; Ashburn, S.; Wills, K. S.; Harvey, K.; Chang, M. C. *J. Appl. Phys.* **2000**, *87*, 1485.

(32) Berweger, S.; Blanchard, P. T.; Brubaker, M. D.; Coakley, K. J.; Sanford, N. A.; Wallis, T. M.; Bertness, K. A.; Kabos, P. *Appl. Phys. Lett.* **2016**, *108*, 073101.

(33) Wagner, T.; Beyer, H.; Reissner, P.; Mensch, P.; Riel, H.; Gotsmann, B.; Stemmer, A. *Beilstein J. Nanotech.* **2015**, *6*, 2193.

(34) Koren, E.; Berkovitch, N.; Azriel, O.; Boag, A.; Rosenwaks, Y.; Hemesath, E. R.; ; Lauhon, L. J. *Appl. Phys. Lett.* **2011**, *99*, 223511.

(35) MacDonald, G. A.; Yang, M.; Berweger, S.; Kabos, P.; Berry, J. J.; Zhu, K.; Del-Rio, F. W. *Energ. Environ. Sci.* **2016**, *9*, 3642.

(36) Gramse, G.; Kölker, A.; Lim, T.; Stock, T. J. Z.; Solanki, H.; Schofield, S. R.; Brincotti, E.; Aeppli, G.; Kienberger, F.; Curson, N. J. *Sci. Adv.* **2017**, *3*, e1602586.

(37) Liu, Y.; Wu, W.; Goddard, III, W. *J. Am. Chem. Soc.* **2018**, *140*, 550.

Graphical TOC Entry